The Galactic neutron star population – II. Systemic velocities and merger locations of binary neutron stars

Nicola Gaspari ![ORCID],[1][*] Andrew J. Levan,[1,2] Ashley A. Chrimes ![ORCID][1,3] and Gijs Nelemans[1,4,5]

[1]*Department of Astrophysics/IMAPP, Radboud University, PO Box 9010, NL-6500 GL Nijmegen, the Netherlands*
[2]*Department of Physics, University of Warwick, Coventry CV4 7AL, UK*
[3]*European Space Agency (ESA), European Space Research and Technology Centre (ESTEC), Keplerlaan 1, NL-2201 AZ Noordwijk, the Netherlands*
[4]*SRON, Netherlands Institute for Space Research, Niels Bohrweg 4, NL-2333 CA Leiden, the Netherlands*
[5]*Institute of Astronomy, KU Leuven, Celestijnenlaan 200D, B-3001 Leuven, Belgium*

ABSTRACT

The merger locations of binary neutron stars (BNSs) encode their galactic kinematics and provide insights into their connection to short gamma-ray bursts (SGRBs). In this work, we use the sample of Galactic BNSs with measured proper motions to investigate their kinematics and predict their merger locations. Using a synthetic image of the Milky Way and its Galactic potential we analyse the BNS mergers as seen from an extragalactic viewpoint and compare them to the location of SGRBs on and around their host galaxies. We find that the Galactocentric transverse velocities of the BNSs are similar in magnitude and direction to those of their Local Standards of Rest, which implies that the present-day systemic velocities are not isotropically oriented and the peculiar velocities might be as low as those of BNS progenitors. Both systemic and peculiar velocities fit a lognormal distribution, with the peculiar velocities being as low as $\sim$22–157 km s^{-1}. We also find that the observed BNS sample is not representative of the whole Galactic population, but rather of systems born around the Sun's location with small peculiar velocities. When comparing the predicted BNS merger locations to SGRBs, we find that they cover the same range of projected offsets, host-normalized offsets, and fractional light. Therefore, the spread in SGRB locations can be reproduced by mergers of BNSs born in the Galactic disc with small peculiar velocities, although the median offset match is likely a coincidence due to the biased BNS sample.

Key words: binaries: general – gamma-ray burst: general – stars: neutron – Galaxy: stellar content – Galaxy: structure.

1 INTRODUCTION

The merger of a binary neutron star (BNS) can manifest itself with a variety of transient phenomena. This includes short-duration gamma-ray bursts (SGRBs) and their afterglows, gravitational waves, and kilonovae, as shown by the multimessenger observations of GW 170817 (Abbott et al. 2017). Although all of these transients can be used to inform the physics of the mergers (Lee & Ramirez-Ruiz 2007; Nakar 2007; Metzger 2017), SGRBs occupy a privileged position due to their luminosity, which makes them the easiest to detect (Metzger & Berger 2012; Burns 2020). Consequently, SGRBs provide the largest sample for analysis, and to date we have more than three decades of literature that explores their connection to BNS mergers (Eichler et al. 1989; Narayan, Paczynski & Piran 1992; for reviews see Berger 2014). The evidence supporting BNS mergers as progenitors are both indirect, such as the lack of association with supernovae, the redshift distribution, the demographics and location of their host galaxies (Berger 2014), and direct, namely the concurrent detection of GRB 170817A and GW 170817. It is important to note, however, that BNS mergers do not have a one-to-one relation

with SGRBs, since it is likely that not all SGRBs are produced by BNS mergers (Thompson & Duncan 1995; Qin et al. 1998; Levan et al. 2006; Metzger, Quataert & Thompson 2008; Troja et al. 2008; Gompertz, Levan & Tanvir 2020), and not all mergers produce an SGRB (Rastinejad et al. 2022; Salafia et al. 2022; Sarin et al. 2022).

A key piece of evidence connecting BNS mergers to SGRBs is their location within the host galaxy. Upon their formation in core-collapse supernovae, neutron stars (NSs) receive natal kicks, as evidenced by the observed peculiar velocities of young Galactic pulsars (Hobbs et al. 2005; Verbunt, Igoshev & Cator 2017). When the NS is in a binary, the natal kick adds to the systemic recoil due to the mass-loss (also known as Blaauw kick, Blaauw 1961; Boersma 1961), and results in a kick to the binary barycentre of up to several hundred km s^{-1} (Tauris et al. 2017; Vigna-Gómez et al. 2018; Andrews & Zezas 2019). Combined with the gravitational-wave in-spiral time, which can be as long as several Gyr or more, BNS can therefore migrate and merge well outside their host galaxy of origin (Bagot, Portegies Zwart & Yungelson 1998; Portegies Zwart & Yungelson 1998; Bloom, Sigurdsson & Pols 1999; Fryer, Woosley & Hartmann 1999; Perna & Belczynski 2002; Voss & Tauris 2003; Belczynski et al. 2006; Zemp, Ramirez-Ruiz & Diemand 2009; Church et al. 2011; Behroozi, Ramirez-Ruiz & Fryer 2014; Mandhai et al. 2022). This is observed in the host-offset distribution of SGRBs, which

---

[*] E-mail: nicola.gaspari@ru.nl

occur at larger projected radii from their hosts than any other class of transient (Fong, Berger & Fox 2010; Fong & Berger 2013; Zevin et al. 2020; Fong et al. 2022), and it is not expected in other progenitor scenarios (e.g. Fryer, Woosley & Hartmann 1999; Berger 2011; Behroozi, Ramirez-Ruiz & Fryer 2014). Nevertheless, a modest fraction (∼20 per cent) of SGRBs are apparently 'hostless' (namely there is no underlying galaxy nor a single galaxy to clearly assign as their host), and although this is not at odds with BNS mergers, it leaves open questions about the nature of largest offsets (Berger 2010; Tunnicliffe et al. 2014; O'Connor et al. 2022). Possible explanations are that BNSs received high systemic kicks (O'Connor et al. 2022), received low systemic kicks (Beniamini & Piran 2016) but were born either in globular clusters (GCs; Grindlay, Portegies Zwart & McMillan 2006; Lee, Ramirez-Ruiz & van de Ven 2010; Church et al. 2011) or in the outer regions of the host (Perets & Beniamini 2021), or that they simply reside in a faint and/or distant host which has not been correctly identified (e.g. Levan et al. 2007).

Understanding the merger locations of BNSs is also important in the context of Galactic chemical enrichment. BNS mergers are thought to be important sites for the production of r-process elements (Eichler et al. 1989; Freiburghaus, Rosswog & Thielemann 1999; Rosswog et al. 1999; Kasen et al. 2017; Pian et al. 2017; for reviews see Cowan et al. 2021) due to the neutron-rich ejecta and kilonovae they produce. There have been efforts to understand Galactic r-process enrichment in the context of BNS mergers in the Milky Way (Symbalisty & Schramm 1982; Eichler et al. 1989; Freiburghaus, Rosswog & Thielemann 1999; Argast et al. 2004; Matteucci et al. 2014; Shen et al. 2015; van de Voort et al. 2015; Wehmeyer, Pignatari & Thielemann 2015; Beniamini, Hotokezaka & Piran 2016; Côté et al. 2018, 2019; Hotokezaka, Beniamini & Piran 2018; Kobayashi et al. 2023), and r-process deposition on Earth has also been linked to kilonovae in the local few kpc (Bartos & Márka 2019; Wang et al. 2021). Therefore, understanding the locations of BNS mergers has wide-ranging implications.

In this paper, we combine two approaches to studying BNS mergers – the locations of SGRBs, and the Galactic BNS population. We evolve a sample of Galactic BNSs forwards in time through the Galactic potential to determine their future merger locations. We place the merger locations in the context of the Milky Way as seen externally, and compare these results with observations of SGRBs in and around their host galaxies. The paper is structured as follows. In Section 2 we describe our Galactic BNS sample, model for the Galactic potential, and a prescription for producing a synthetic Milky Way image. Section 3 analyses the present-day velocities of observed Galactic BNSs and discusses their implications for birth locations and velocities. Section 4 presents results for BNS merger locations and their measurements as viewed from afar. Section 5 outlines possible systematics in the methodology, before we summarize and conclude in Section 6.

Throughout, magnitudes are reported in the AB system (Oke & Gunn 1982), and a flat Lambda cold dark matter cosmology is adopted with $H_0 = 70$ km s^{-1} Mpc^{-1} and $\Omega_m = 0.3$.

2 MODELS

2.1 Merger locations of the Galactic BNSs

We collected our sample of Galactic BNSs from the ATNF catalogue (Manchester et al. 2005),[1] and their properties are summarized in

Table 1 along with the estimated merger times τ_{gw} for a gravitational-radiation-driven inspiral (Peters 1964). Out of the 15 confirmed BNSs (we exclude possible NS–WD binaries), eight have measured proper motions, and five have both proper motions and $\tau_{gw} < 14$ Gyr. Since our primary objective is to make predictions about BNSs merging within an Hubble time, only the last five are employed in our fiducial models. The remaining BNSs are used to test for systematic effects in our methodology.

To predict the BNSs merger locations we produce 10^4 realizations of the Galactic trajectory of each binary, starting from as many realizations of their present-day positions and velocities. These initial conditions are generated through a Monte Carlo (MC) simulation, which employs observational uncertainties and allows us to propagate them to the predicted merger locations.

2.1.1 Initial positions and velocities

To compute the BNSs initial positions, we assume that right ascension, declination, and distance follow Gaussian distributions with mean equal to the estimated values and standard deviation equal to the respective uncertainties. These distributions are sampled 10^4 times for each binary, giving as many realizations of their initial position.

The distances listed in Table 1 without uncertainties are estimates obtained from the dispersion measure (DM) using the electron-density model of Yao, Manchester & Wang (2017). For J0453+1559, J1411+2551, and J1518+4904, we also report the DM distances obtained with the model of Cordes & Lazio (2002), which will be used in Section 5.1 for comparison. On the DM distances we assume a conservative 20 per cent uncertainty, as done by Tauris et al. (2017). For B2127+11C, as it is likely bound to the GC NGC 7078 (Kirsten et al. 2014), we assume its position to be that of the GC (see Table 2). Another exception is made for the distances of J0737−3039A/B and J1756−2251, for which we use the non-Gaussian probability distributions given by Verbiest et al. (2012).[2] The BNS present-day positions are shown in Galactocentric coordinates in Fig. 1.

To compute the BNS initial velocities, we apply the same MC approach to the proper motions in right ascension and declination. We assume that the proper motions have Gaussian uncertainties with standard deviation equal to the observational uncertainties, and we produce 10^4 realizations for each binary. Each realization is then converted to linear units (i.e. km s^{-1}) using one of the distance realizations, and the transverse component of the Sun's velocity is added to obtain the BNS transverse velocity V_t in the Galactocentric frame. Since we have no observational estimates for the radial velocities V_r but for B2127+11C (for which we use the radial velocity of NGC 7078), we obtain the 3D velocities through an MC simulation of their orientations θ with respect to the line of sight (LoS).

For our fiducial models, we assume that the BNSs systemic velocities are isotropically oriented in the Galactocentric frame, and we hence compute V_r as

$$V_r = V_t \cot \theta, \tag{1}$$

where $\theta = \arccos u$ and u is a real value uniformly sampled 10^4 times between 0 and 1. Hereafter, we will refer to the systemic velocities obtained with this assumption as Galactocentric-isotropic velocities. If the sample were bigger, we could test the isotropy assumption e.g. by comparing the mean value of 1D velocities to that of 2D velocities,

---

[1]http://www.atnf.csiro.au/research/pulsar/psrcat

[2]http://psrpop.phys.wvu.edu/LKbias/

Table 1. BNS sample used in this work. The columns list the pulsar, the right ascension and declination, the proper motion in right ascension and declination, the distance from the Sun, the merger time, and the references for the listed values. Values in parenthesis are the uncertainties in the preceding digits.

Radio pulsar	RA [deg]	Dec. [deg]	μ_α [mas yr^{-1}]	μ_δ [mas yr^{-1}]	Dist. [kpc]	$\tau_{\rm gw}$ [Myr]	Ref.
J0737−3039A/B	114.46353508(11)	−30.66130953(3)	−3.82(62)	2.13(23)	1.1(1,2)	85	(a)
B1534+12	234.291507208(13)	11.932064964(17)	1.482(7)	−25.285(12)	1.051(5)	2735	(b)
J1756−2251	269.19430755(7)	−22.866486(6)	−2.42(8)	0(20)	0.73(24,60)	1457	(c)
B1913+16	288.86666425(13)	16.10760744(14)	−0.72(11)	−0.03(14)	4.1(7,20)	301	(d)
B2127+11C[a]	322.5050175(5)	12.1772803(12)	−1.3(5)	−3.3(10)	25.000	215	(e)
J0453+1559	73.4392237(3)	15.9892517(17)	−5.5(5)	−6.0(42)	0.522[b] − 1.07[c]	1 456 721	(f)
J1411+2551	212.828608(13)	25.852331(20)	−3(12)	−4(9)	1.131[b] − 0.98[c]	>465446	(g)
J1518+4904	229.56999618(7)	49.07618089(5)	−0.67(4)	−8.53(4)	0.964[b] − 0.63[c]	>8826539	(h)
J0514−4002A[a,d]	78.5278863(9)	−40.0469147(6)	5.19(22)	−0.56(25)	25.000	507 733	(i)
J0509+3801	77.3824504(11)	38.021690(4)	–	–	1.562[b]	579	(j)
J1757−1854	269.2657683(3)	−18.9009378(20)	–	–	19.559[b]	76	(k)
J1811−1736	272.979308(13)	−17.61047(12)	–	–	4.419[b]	>1794804	(l)
J1829+2456	277.3944450(9)	24.9383869(9)	–	–	0.909[b]	>55375	(m)
J1913+1102	288.3710592(13)	11.034928(3)	–	–	7.140[b]	>465	(n)
J1930−1852	292.623815(3)	−18.862853(17)	–	–	2.004[b]	>1e8	(o)
J1946+2052	296.55888(3)	20.87351(3)	–	–	3.510[b]	>46	(p)
J1753−2240[d]	268.41603(3)	−22.6783(3)	–	–	3.232[b]	–	(q)
J1755−2550[d]	268.910000(17)	−25.8394(5)	–	–	4.891[b]	–	(r)
J1759+5036[d]	269.940300(13)	50.615822(6)	–	–	0.543[b]	>179604	(s)
J1807−2459B[a,d]	271.8369634(3)	−25.000532(5)	–	–	3.045[b]	1 039 373	(t)
J1906+0746[d]	286.70358(17)	7.77386(20)	–	–	7.4(14,25)	309	(u)

Notes. [a]Associated with a GC. [b]Estimated from DM following Yao, Manchester & Wang (2017). [c]Estimated from DM following Cordes & Lazio (2002). [d]Not a confirmed BNS.
References. (a) Burgay et al. (2003); Kramer et al. (2006); Deller, Bailes & Tingay (2009); Verbiest et al. (2012). (b) Stairs et al. (2002); Fonseca, Stairs & Thorsett (2014). (c) Ferdman et al. (2014). (d) Weisberg, Nice & Taylor (2010); Weisberg & Huang (2016); Deller et al. (2018). (e) Jacoby et al. (2006). (f) Martinez et al. (2015). (g) Martinez et al. (2017). (h) Janssen et al. (2008). (i) Ridolfi et al. (2019). (j) Lynch et al. (2018). (k) Cameron et al. (2018). (l) Mignani (2000); Corongiu et al. (2007). (m) Champion et al. (2004, 2005) (n) Lazarus et al. (2016). (o) Swiggum et al. (2015). (p) Stovall et al. (2018). (q) Keith et al. (2009). (r) Ng et al. (2018). (s) Agazie et al. (2021). (t) Lynch et al. (2012). (u) van Leeuwen et al. (2015).

Table 2. Properties of the GCs associated with a Galactic BNS. The columns list the pulsar, the associated GC, the right ascension and declination, the distance from the Sun, the proper motion in right ascension and declination, and the mean radial velocity. The values in parenthesis are the uncertainties in the preceding digits. Data are taken from Baumgardt et al. (2019).

Radio pulsar	GC	RA [deg]	Dec. [deg]	Dist. [kpc]	μ_α [mas yr^{-1}]	μ_δ [mas yr^{-1}]	$V_{\rm r}$ [km s^{-1}]
B2127+11C	NGC 7078	322.493042	12.167001	10.22(13)	−0.63(1)	−3.80(1)	−106.76(25)
J0514−4002A[a]	NGC 1851	78.528160	−40.046555	11.33(19)	2.12(1)	−0.63(1)	320.30(25)
J1807−2459B[a]	NGC 6544	271.835750	−24.997333	2.60(27)	−2.34(4)	−18.66(4)	−38.12(76)

Note. [a]Not a confirmed BNS.

as done for isolated pulsars by Hobbs et al. (2005). However, the small sample size prevents us from doing so, hence the sole purpose of this assumption is to best reflect our ignorance about the radial velocities.

We also provide a second estimate for the radial velocities, obtained assuming that the peculiar velocities in the BNSs Local Standards of Rest (LSRs) are isotropically oriented. Here, we define as BNS LSR the frame of reference centred on the BNS location, and moving on a circular orbit around the Z-axis of the Galactocentric frame. Under this assumption, we get $V_{\rm r}$ by first subtracting the LSR transverse velocity vector $\mathbf{V}_{\rm t,\ LSR}$ from the BNS transverse velocity vector $\mathbf{V}_{\rm t}$, and then computing $V_{\rm r}$ from the residuals, namely

$$V_{\rm r} = \|\mathbf{V}_{\rm t} - \mathbf{V}_{\rm t,\ LSR}\| \cot\theta + V_{\rm r,LSR}, \qquad (2)$$

where $V_{\rm r,LSR}$ is the BNS LSR radial velocity. Hereafter, we refer to these realizations as LSR-isotropic velocities. This second estimate is motivated by the possibility that Galactic BNSs might receive

small systemic kicks from the second supernova (Beniamini & Piran 2016), which would result in small peculiar velocities (Andrews & Zezas 2019). The systemic velocities V and the peculiar velocities $V^{\rm LSR} = \|\mathbf{V} - \mathbf{V}_{\rm LSR}\|$ obtained under the two assumptions are shown in Fig. 2.

The initial conditions are computed using the default values for the Sun Galactocentric position and velocity from ASTROPY v4.0[3] (Astropy Collaboration 2022).

2.1.2 Galactic trajectories

The Galactic trajectories defined by each realization of initial position and velocity are computed with GALPY[4] (Bovy 2015) using the Galactic potential model of McMillan (2017). The trajectories are

[3]http://www.astropy.org
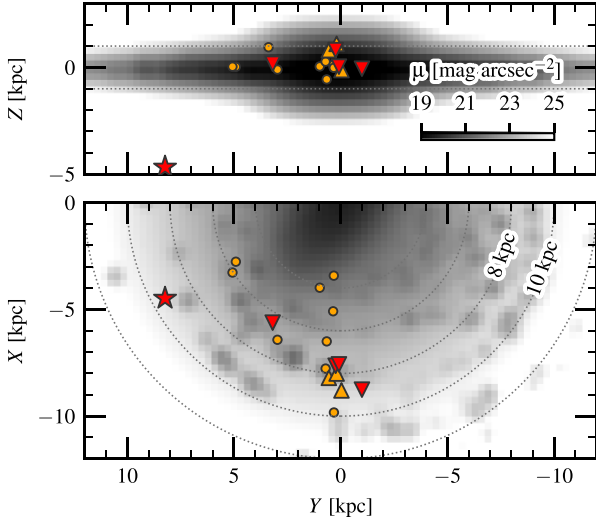[4]https://github.com/jobovy/galpy

Figure 1. Present-day positions of the Galactic BNSs over a synthetic Milky Way image. The triangles indicate binaries with measured proper motions, while the red markers indicate binaries merging within a Hubble time. The dots indicate binaries without measured proper motions. The star-shaped marker indicates B2127+11C, which is associated with the GC NGC 7078. The underlying image is our fiducial model for a Milky Way image if it were located at $z = 0.5$ and observed with a PSF FWHM of 0.1 arcsec, and a pixel size of 0.05 arcsec px^{-1} (see Section 2.2 for details). The centre of the edge-on image reaches 18.3 mag arcsec^{-2}, and both images are cut at a limiting surface brightness of 25 mag arcsec^{-2}.

evolved up to the merger time τ_{gw} of the respective binary, and the final positions are assumed to be the merger location. As we start from 10^4 initial conditions for each BNS, we end up with the same number of merger locations.

2.2 Synthetic image of the Milky Way

To analyse the BNS merger locations in the same way as SGRBs on their host, we need to reproduce how the Milky Way appears from a cosmological distance. To do so, we employ the Milky Way synthetic image of Chrimes et al. (2021), upgrading their 2D face-on model to 3D so that we can include the effects of a random viewing angle.

2.2.1 Model structure: bulge, disc, and spiral arms

In the following section, we provide a brief overview of the Galactic components combined to create the synthetic image, while a thorough description can be found in Chrimes et al. (2021).

The bar-bulge is modelled with the triaxial boxy Gaussian distribution fitted on Mira variables by Grady, Belokurov & Evans (2020), i.e.

$$\rho_{bar} = \rho_{b,0} \exp(-0.5m^2), \tag{3}$$

where

$$m = \left\{ \left[\left(\frac{x}{X_b} \right)^2 + \left(\frac{y}{Y_b} \right)^2 \right]^2 + \left(\frac{z}{Z_b} \right)^4 \right\}^{\frac{1}{4}} \tag{4}$$
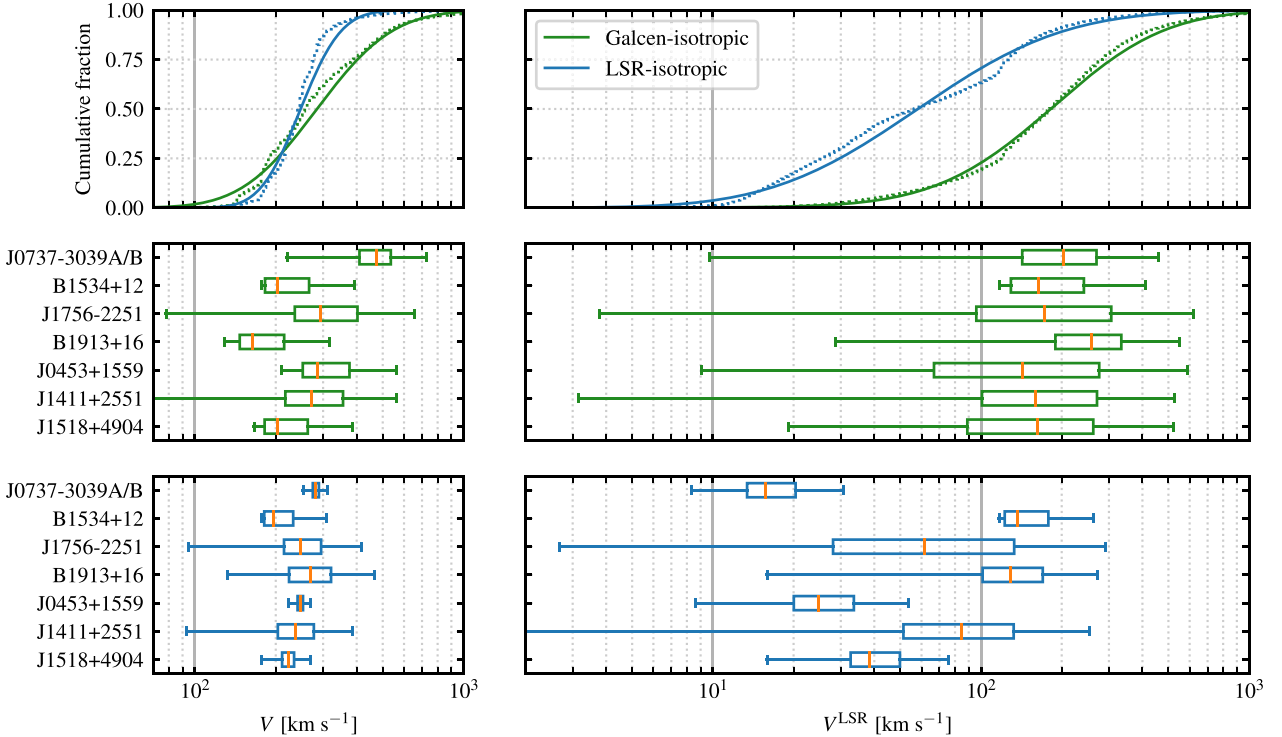

Figure 2. Galactocentric systemic velocities V and peculiar velocities in the BNS LSRs V^{LSR} of the Galactic BNSs with measured proper motions (except B2127+11C). The upper panels show the total cumulative distributions of V and V^{LSR}. The dashed lines are distributions from the MC simulations, while the solid lines are lognormal distribution fitted to the MC simulations. The middle and bottom panels show, respectively, the Galactocentric-isotropic and LSR-isotropic velocities for each single BNS considered. The boxes extend from the first to the third quartiles, with the orange line on the median value.

with $(X_b, Y_b, Z_b) = (2.05, 0.95, 0.73)$ kpc, and $\rho_{b,0}$ is the normalization factor. The angle between the bar-bulge semimajor axis and the Galactic-Centre LoS is assumed to be $27°$ (Wegg & Gerhard 2013).

The disc is modelled with a double exponential disc

$$\rho_{disc} = \rho_{d,0} \exp\left(-\frac{\sqrt{x^2 + y^2}}{R_d}\right) \exp\left(-\frac{|z|}{Z_d}\right), \tag{5}$$

where $R_d = 2.6$ kpc and $Z_d = 0.3$ kpc. These scale values are typical estimates for the Milky Way thin disc, which is the dominant component of the disc stellar light (Bland-Hawthorn & Gerhard 2016).

The spiral arms are mapped following the method of Reid et al. (2019), using young stellar object masers and H II regions from Urquhart et al. (2014) as tracers. To avoid the shadow produced by dust absorption behind the bar-bulge, we only use the lower half of the map, at Galactocentric coordinates $X \leq 0$ (see Fig. 1), while the upper half is replaced by a reflected lower half.

The synthetic images are produced in two bands, namely the *I* and the *B* band. The normalization factors $\rho_{b,0}$ and $\rho_{d,0}$ are tuned so that the total luminosity of the respective components matches the observational estimates. In the *I* band we match the luminosities given by Flynn et al. (2006), namely $10^{10} L_\odot$ for the bar-bulge, and $3 \times 10^{10} L_\odot$ for the disc including spiral arms. For the *B* band we use instead the $B - I$ colours of Milky Way analogues from Licquia, Newman & Brinchmann (2015). We use $B - I = 2.41$ for the bulge-bar and $B - I = 1.62$ for the disc including arms, which give, respectively, a total luminosity of $0.11 \times 10^3 L_\odot$ and $0.67 \times 10^3 L_\odot$. The *I*-band luminosities are corrected for dust extinction, while the *B*-band luminosities are not (for details see Chrimes et al. 2021).

The fraction of disc luminosity arising from the spiral arms alone is assumed to be equal to the arm strength, which is the relative amplitude of the second- to fourth-order Fourier components of the azimuthal light profile along elliptical isophotes (e.g. Yu et al. 2018). For the *I* band we use an arm strength of 0.15 (e.g. Díaz-García et al. 2019; Yu & Ho 2020), while for the *B* band we use 0.20 (Yu et al. 2018), both of which are typical values for Milky Way analogues.

2.2.2 Photometry and half-light radius

The method described in the previous section gives an analytical model of the Milky Way luminosity density in units of e.g. $L_\odot\,pc^{-3}$. To produce a 2D image, the model is first projected along an arbitrary LoS, then processed to mimic the effects of redshift and instrumental resolution to simulate observations with a given instrument of the galaxy as viewed at an arbitrary redshift.

We start with a grid of points in Galactocentric coordinates. The grid is rotated by a phase ϕ along the *Z*-axis and by a inclination *i* along the *Y*-axis, in order to be aligned with the chosen LoS. The analytical 3D model is evaluated on the grid and summed along the *X*-axis with a Riemann sum, to get a 2D image of the surface brightness *I* in units of $L_\odot\,pc^{-2}$. The number of grid points is chosen such that a double Riemann sum of the image gives a total luminosity differing by less than 1 per cent from the prescribed value.

We then chose the observer redshift *z*, the point spread function (PSF), and the pixel scale of the image (i.e. the angular resolution). The 2D grid is converted from linear to angular units (e.g. from pc to arcsec) using the angular diameter distance $D_A(z)$, and the image is first convolved with a Gaussian PSF of given full width at half-maximum (FWHM) and then downsampled to the pixel scale. The last step is done using `measure.block_reduce` from the

`scikit-image` library (van der Walt et al. 2014). For the fiducial models we use $z = 0.5$, a pixel size of $0.05\,arcsec\,px^{-1}$, and a PSF FWHM of 0.1 arcsec. The fiducial redshift is chosen because the median redshift of our SGRB sample is $z = 0.46$, while the other two values are typical for the SGRB hosts observations, for which the comparison sample used here is predominantly taken via the *Hubble Space Telescope* (*HST*, see Table 4 for references). The possible systematics introduced by this choice of parameters are discussed in Section 5.4.

For our purposes, namely computing half-light radii and fractional fluxes, we need to measure the Galaxy total flux from the images. Since its value depends on the image depth, we need to simulate the background noise. To do so, we first convert *I* from $L_\odot\,pc^2$ to $L_\odot\,arcsec^2$ using the angular distance D_A. Then, we convert the surface brightness from $L_\odot\,arcsec^2$ to $mag\,arcsec^2$ using

$$\mu = -2.5 \log I + 5 \log\left(\frac{D_L}{10\,pc}\right) - 2.5\log(1 + z) + M_\odot, \tag{6}$$

where μ is the surface brightness in magnitude units, $D_L(z)$ is the luminosity distance, and $M_\odot$ is the absolute magnitude of the Sun, i.e. 4.51 in the *I* band and 5.31 in the *B* band (Willmer 2018). Finally, we chose a limiting magnitude μ_{lim} and set to $I = 0$ and $\mu = \mu_{lim}$ all those pixels with $\mu > \mu_{lim}$. In our fiducial models we use $\mu_{lim} = 25\,mag\,arcsec^2$, motivated again by the typical values of the SGRB host observations. The edge-on and face-on images obtained with the fiducial set-up are shown in Fig. 1.

The half-light radius r_e is given as the semimajor axis of the isophote enclosing half of the total flux. We use elliptical isophotes, fitted using `isophote.Ellipse.fit_image` from the `photutils` package (Bradley et al. 2023).

3 SYSTEMIC AND PECULIAR VELOCITIES

Before analysing the merger locations, it is worth taking a closer look at the BNS present-day velocities, as they bear some insight not only about the predicted merger locations but also about the BNS properties themselves. In the following section we consider the seven BNSs with measured proper motion, with the exception of B2127+11C, which is likely bound to a GC, and thus has a proper motion which might be biased by the GC internal dynamics.

3.1 Transverse velocity of the BNSs and their LSR

Let us consider the BNS transverse velocities $\mathbf{V}_t$. When we compare them to the transverse velocities of their respective LSRs $\mathbf{V}_{t,\,LSR}$ (namely the circular velocity at their position), we find that the two have similar magnitudes and directions in all but two cases (see Fig. 3). This suggests that the BNS systemic velocities are (i) not isotropically oriented in the Galactocentric frame, and (ii) not much different from the velocity of their LSR, or in other words, they have small peculiar velocities with respect to their LSR. From Fig. 3, we notice that this is due to the tangential component of the Sun's velocity $\mathbf{V}_{t,\odot}$ being aligned to $\mathbf{V}_{t,\,LSR}$ and dominating over the BNS proper motions. We also notice that $\mathbf{V}_{t,\,LSR}$ are almost completely in the tangential direction, since $V_{t,\,LSR}$ is ~ 200 km s^{-1} in all but two cases.

For the reason discussed in the previous paragraph, we conclude that the BNS systemic velocities inferred under the assumption of Galactocentric-isotropy (equation 1) might be overestimated.
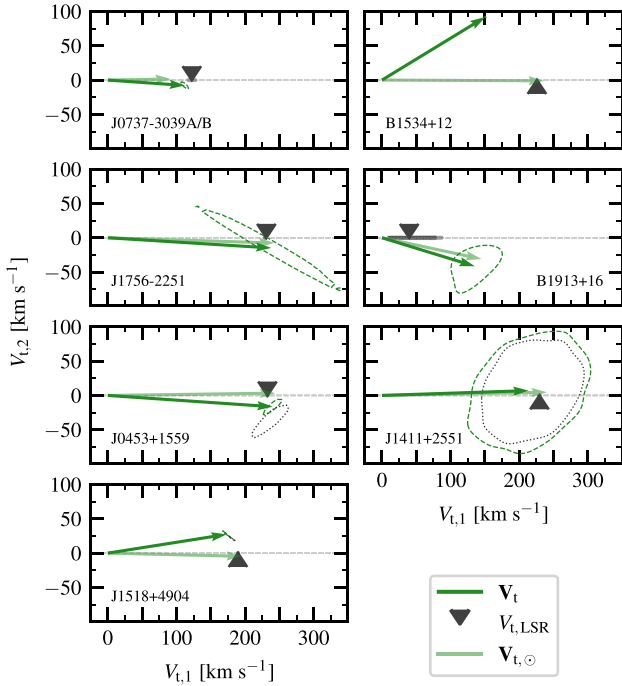
Figure 3. Transverse velocities of the BNSs in Fig. 2. The axes are arbitrarily oriented so that the LSR transverse velocity vectors $\mathbf{V}_{\mathrm{t,\,LSR}}$ lie on the x-axis. The grey triangles indicate the LSR transverse velocities $V_{\mathrm{t,\,LSR}}$, green arrows indicate the BNSs transverse velocities $\mathbf{V}_{\mathrm{t}}$, and the light-green arrows indicate the transverse component of the Sun velocity $\mathbf{V}_{\mathrm{t,\,\odot}}$. The dashed green lines enclose the 1σ regions of $\mathbf{V}_{\mathrm{t}}$, while the grey shaded areas are the 1σ regions of $V_{\mathrm{t,\,LSR}}$, both obtained from a Gaussian kernel density estimation of our MC simulations. These 1σ regions represent the uncertainties from the on-sky locations and proper motions, and the distance estimates. The dotted black lines of J0453+1559, J1411+2551, and J1518+4904 enclose the $\mathbf{V}_{\mathrm{t}}$ 1σ regions when the DM distance is estimated from Cordes & Lazio (2002) instead of Yao, Manchester & Wang (2017).

Instead, those inferred under the assumption of LSR-isotropy (equation 2) likely provide a lower limit, since similar $\mathbf{V}_{\mathrm{t}}$ and $\mathbf{V}_{\mathrm{t,\,LSR}}$ would result in small radial velocities. This becomes clear when comparing the systemic and peculiar velocities V and V^{LSR} from the two assumptions. In the middle and bottom panels of Fig. 2 we see that while we obtain similar V from the two assumptions, the Galactocentric-isotropic V^{LSR} all peak around $\sim$200 km s^{-1}, whereas the LSR-isotropic ones are distributed between $\sim$10 and $\sim$200 km s^{-1}. These latter estimates cover the same range of values as the BNS progenitors, namely NS-hosting high-mass X-ray binaries (see fig. 2 from Fortin et al. 2022), and that they get as low as the velocity dispersion in the thin disc (Robin et al. 2003).

The cumulative distributions of V and V^{LSR} for all the BNSs with measured proper motions (except the one in the GC, i.e. B2127+11C) are fitted with the lognormal distribution

$$f(x, \alpha, \beta, \gamma) = \frac{1}{x\beta\gamma\sqrt{2\pi}} \exp\left[-\frac{1}{2\gamma^2}\log^2\left(\frac{x-\alpha}{\beta}\right)\right] \qquad (7)$$

using `scipy.stats.lognorm.fit` (Virtanen et al. 2020). The fits are shown in the upper panels of Fig. 2 and the fitted parameters are reported in Table 3. For the whole sample, we find $V \approx 285^{+190}_{-113}$ km s^{-1} and $V^{\mathrm{LSR}} \approx 182^{+209}_{-100}$ km s^{-1} under Galactocentric-isotropy, and $V \approx 245^{+81}_{-56}$ km s^{-1} and $V^{\mathrm{LSR}} \approx 58^{+99}_{-36}$ km s^{-1} under LSR-

isotropy. This lower value is also consistent with that inferred by Beniamini & Piran (2016).

Despite the qualitative differences resulting from the two assumptions, we do not expect them to produce quantitative differences in the merger locations. Indeed, both assumptions result in systemic velocities that are close to the circular velocity ($\sim$230 km s^{-1}, Bovy et al. 2012; McMillan 2017) and well below the escape velocity at the Sun location ($\sim$500–600 km s^{-1}, Piffl et al. 2014; Monari et al. 2018). Therefore, they should lead to similar merger offsets. A quantitative analysis of their effect on the results is provided in Section 5.2.

3.2 Implications for birth locations and velocities

As mentioned in the previous section, almost all the BNSs with proper motions have $\mathbf{V}_{\mathrm{t}}$ closely aligned to $\mathbf{V}_{\mathrm{t,\,LSR}}$, which hints that $\mathbf{V}$ is likely not isotropic. The deviation is evident when comparing the angles θ between $\mathbf{V}_{\mathrm{t}}$ and $\mathbf{V}_{\mathrm{t,\,LSR}}$ to the isotropic distribution, as shown in the left-hand panel of Fig. 4. The $\mathbf{V}_{\mathrm{t}} - \mathbf{V}_{\mathrm{t,\,LSR}}$ alignment also implies that the BNSs might have peculiar velocities V^{LSR} as low as those of their progenitors. This in turn suggests that our sample might be biased towards systems that received low kicks to the barycentre following the second supernova, and raises the question about how low the kicks should be in order to reproduce the observed θ.

To this end, we employ a toy model to check the range of suitable kicks. We simulate the trajectories of 10^5 point masses with circular orbits in the Galactic disc after receiving a kick $V_{\mathrm{in}}^{\mathrm{LSR}}$. We test seven different kick magnitudes, namely 50, 100, 200, 300, 400, 500, and 600 km s^{-1}, and for each of these values we seed the point masses in the plane at $Z = 0$ using equation (5) as probability distribution. The masses are initialized with a velocity equal to the circular velocity plus a kick $V_{\mathrm{in}}^{\mathrm{LSR}}$ in a random direction. The trajectories are integrated for 5 Gyr, and we record location and velocity at 300 random times between 0 and 5 Gyr. Of all the locations we record, we select those that fall within 1 kpc from the Sun since the BNS sample is biased to this region, and compute the angle θ_{fin} between $\mathbf{V}_{\mathrm{t}}$ and $\mathbf{V}_{\mathrm{t,\,LSR}}$. The respective starting radial positions R_{in} are recorded as well.

The left-hand panel of Fig. 4 shows a comparison between the measured θ distribution and the predicted θ_{fin} distributions for each value of $V_{\mathrm{in}}^{\mathrm{LSR}}$. We find that lower kicks result in angles skewed towards small values (meaning $\mathbf{V}_{\mathrm{t}}$ is mostly aligned to $\mathbf{V}_{\mathrm{t,\,LSR}}$), while at higher kicks the angle distribution steepens at both low and high values (meaning $\mathbf{V}_{\mathrm{t}}$ is either aligned or anti-aligned to $\mathbf{V}_{\mathrm{t,\,LSR}}$). The measured θ distribution is well reproduced with kick magnitudes up to 100–200 km s^{-1}, which are compatible with the values inferred from the observed SGRB offsets ($\sim$20–140 km s^{-1}, Fong & Berger 2013). We find that strongly kicked systems probe the inner regions of the Galaxy, while weakly kicked systems probe only a region close to the Sun, as shown in the middle panel in Fig. 4.

Since each realization with different kicks in the disc start with the same number of binaries, the right-hand panel of Fig. 4 shows that the number of binaries with 1 kpc of us in the strong-kick scenarios is <40 per cent of the weak-kick scenarios. Therefore a modest population of strongly kicked binaries would not be recovered in the BNS samples that we have to date. Taking into account that population synthesis predicts an anticorrelation between kicks and merger times (e.g. fig. C1 in Vigna-Gómez et al. 2018), hence that strongly kicked BNSs should be even rarer in the Milky Way given its age and low star formation rate, the $\mathbf{V}_{\mathrm{t}} - \mathbf{V}_{\mathrm{t,\,LSR}}$ alignment suggests that our sample probes only the BNS population born with small $V_{\mathrm{in}}^{\mathrm{LSR}}$ at around the same Galactocentric radius as the Sun. In other

Table 3. Parameters of the lognormal distributions fitted to systemic velocities V and peculiar velocities V^{LSR}. The last four rows report median values μ and 16th–84th percentiles, using DM distances from either Yao, Manchester & Wang (2017) (two upper rows) or Cordes & Lazio (2002) (two lower rows) for J0453+1559, J1411+2551, and J1518+4904.

	V		V^{LSR}	
	Galcen-iso	LSR-iso	Galcen-iso	LSR-iso
α	8.48	21.35	−11.14	0.46
β	276.16	226.13	192.91	57.66
γ	0.53	0.30	0.74	1.01
μ [km s^{-1}]	285	245	182	58
1σ [km s^{-1}]	172–475	189–326	82–391	22–157
μ [km s^{-1}]	284	247	182	60
1σ [km s^{-1}]	175–474	192–323	83–391	23–159

words, that our sample is neither representative of the BNSs born in the central regions, nor of the BNSs residing in the outer regions of the Milky Way.

4 MERGER LOCATIONS

In the following sections we analyse the merger locations of the five Galactic BNSs with measured proper motions and $\tau_{gw} < 14$Gyr, over the fiducial Milky Way image in the I band. We refer to this set-up as the fiducial model. The analysis employs three observables: the projected offsets r_h, the normalized offset r_n, and the fraction of light f_{light}. The first observable is the on-sky projection of the merger offset from the Galactic Centre, the second is the projected offset expressed in units of r_e, and the third is the fraction of total light contained in pixels dimmer than the one at the transient location. The last two observables are commonly used in the analysis of transients locations on their hosts (e.g. Bloom, Kulkarni & Djorgovski 2002; Fruchter et al. 2006), including SGRBs (e.g. Berger 2014).

We choose the viewing angles with which to project the 3D galaxy model on to a 2D image, for each merger, from an isotropic

distribution. The possible values for i and ϕ are distributed over a discrete grid with 10 values for i and 20 for ϕ. In particular, we use $i = \arccos(u)$ where the u are 10 evenly spaced values in [0,1], and ϕ are 20 evenly spaced values in $[0, \pi]$.

The predictions are then compared to a sample of observed SGRBs, listed in Table 4. The sample is a subset of the SGRBs analysed by Fong et al. (2022), selected for having measured r_n. The f_{light} values are collected from various works in the literature (see Table 4 for the references).

4.1 Projected offsets

We produce 10^4 realizations of the r_h distribution by picking 1 out of the 10^4 merger locations for each of the five Galactic BNSs. The cumulative r_h distributions are shown in the left-hand panels of Fig. 5, together with those of the SGRBs. The latter are produced with an MC simulation, assuming the SGRB offsets in Table 4 have Gaussian uncertainties with standard deviation equal to the observational uncertainties. We produce 10^4 realizations of such distributions, so that we can compare them one-to-one to those of the Galactic BNSs.

The Kolmogorov–Smirnov (KS) test cannot reject the null hypothesis at a significance level below 5 per cent in virtually all realizations. In particular, the null hypothesis is rejected in <0.3 per cent of cases when comparing the BNS mergers to the whole SGRB sample, in <0.5 per cent of cases when comparing to SGRBs with late-types host (type Q and T in Table 4), and in <0.1 per cent when comparing to SGRBs with early-types host (type SF in Table 4). Note that the BNSs merger realizations are not independent, thus one should not expect to reject the null hypothesis at a 5 per cent significance level in ∼5 per cent of cases, as per definition.

The median projected offset of the BNS mergers is $\langle r_h \rangle \approx 6$ kpc (see Fig. 5). This value is similar to the BNS present-day offsets, which due to observational bias is around the Galactocentric radius of the Sun, i.e. $R_\odot \approx 8$ kpc (which is on average 20 per cent smaller
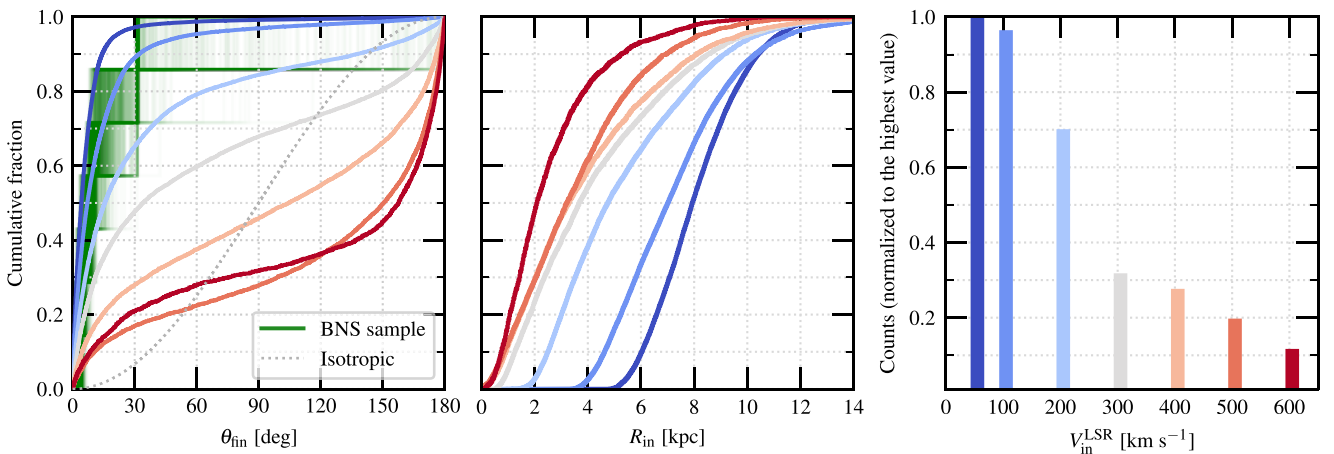

Figure 4. Left. Distribution of angles θ_{fin} between $\mathbf{V}_t$ and $\mathbf{V}_{t, LSR}$ for different kicks V_{in}^{LSR}. The green lines labelled 'BNS sample' are realizations of the observed θ from Galactic BNSs, while all the other solid coloured lines are predictions for binaries in an exponential disc after an isotropic kick of given magnitude, as explained in Section 3.2. The colour code for the kick magnitude V_{in}^{LSR} is shown in the right plot. The grey dotted line is the distribution predicted for point masses with isotropic velocities, located at random positions within 1 kpc from the Sun. **Centre.** Initial radial positions R_{in} of the point masses that end up within 1 kpc of the Sun for different kicks V_{in}^{LSR}. As we can see, high V_{in}^{LSR} allow us to probe the inner Galactic regions, whereas low V_{in}^{LSR} bias the sample to systems with $R_{in} \approx R_\odot$. **Right.** Counts of the point masses that end up within 1 kpc of the Sun for different kicks V_{in}^{LSR}, normalized to the highest value. As V_{in}^{LSR} increases, the systems found around the Sun becomes less numerous.
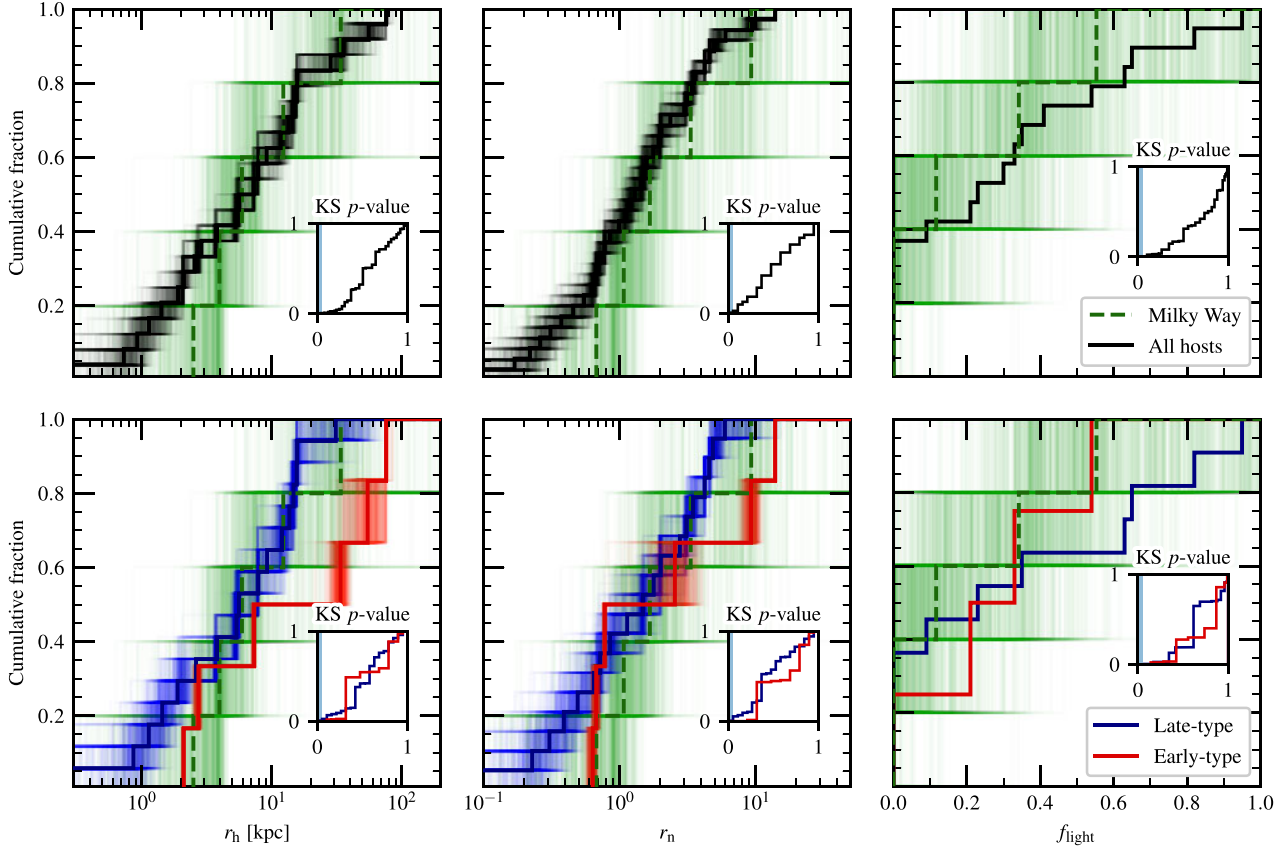
Figure 5. Projected offsets r_h (left), normalized offsets r_n (centre), and fraction of light f_{light} (right) for BNS mergers and SGRBs. The solid thick lines represent the median distributions of SGRBs, either for the whole sample (upper panels) or divided by host type (lower panels). The dashed thick lines represent the median distributions of BNSs mergers from our fiducial model. The semitransparent lines are the single realizations of the corresponding distributions. The insets show the distribution of the p-values from the KS test when comparing all the realizations one-to-one, with the shaded area indicating the 5 per cent region.

upon projection),[5] and it is a result of the systemic velocities being close to the circular velocity, and well below the escape velocity at the Sun location. By chance, these values are similar to the median projected offset of the SGRBs, which is $\langle r_h \rangle \approx 8$ kpc (see Fig. 5). When taken together with the small radial displacement in the BNS trajectories, this suggests that the similarity between the r_h distributions of SGRBs and BNS mergers might be simply a coincidence, resulting from the BNS sample being biased towards systems located close to the Sun. Or in other words, if the Sun were located at a significantly larger (or smaller) Galactocentric radius, then we might find the same BNSs mergers peaking at a different r_h. Nevertheless, it is noteworthy that our models predict merger offsets that are comparable to the upper tail of the SGRB distribution despite this bias.

4.2 Normalized offsets

The cumulative distributions of r_n for the BNS mergers are shown in the middle panels of Fig. 5, together with those for the SGRBs.

---

[5]Consider a point on a sphere with Cartesian coordinates $(x, y, z) = (\rho\cos\phi\sin i, \rho\sin\phi\sin i, \rho\cos i)$. The projected radius on the xy-plane is $R = \rho\sin i$. The expected value of R assuming an isotropic random orientation is $\langle R \rangle = \frac{\int_0^{2\pi} d\phi \int_0^\pi \rho \sin^2 i \, di}{\int_0^{2\pi} d\phi \int_0^\pi \sin i \, di} = \frac{\pi}{4}\rho \approx 0.8\rho.$

Similarly to the r_h, the KS test cannot reject the null hypothesis at a significance level below 5 per cent in virtually all realizations. In particular, the null hypothesis is rejected in <0.5 per cent of cases when comparing the BNS mergers to the whole SGRB sample, in <0.4 per cent of cases when comparing to SGRBs with late-types host, and in <0.1 per cent when comparing to SGRBs with early-types host. Overall, we find that the projected offsets of the various samples agree better when normalized to r_e, as already noted by Nugent et al. (2022).

The inclusion of Milky Way's morphological properties in our analysis, e.g. r_e, raises the question about how representative our Galaxy is with respect to the SGRB host population. Although a thorough comparison is beyond the scope of this work, a brief discussion is already insightful. The Milky Way is a very bright yet relatively red spiral galaxy, which likely belongs to the green valley in the colour–magnitude diagram (Mutch, Croton & Poole 2011; Licquia, Newman & Brinchmann 2015; Boardman et al. 2020). Although its total stellar mass ($M_\star \approx 6 \times 10^{10}$ M$_\odot$, Bland-Hawthorn & Gerhard 2016) is around the median value for transitioning/quiescent (T/Q) SGRB host and 1σ higher than star-forming (SF) hosts, its star formation rate ($\dot{m}_\star \approx 1.65$ M$_\odot$ yr^{-1}, Bland-Hawthorn & Gerhard 2016) is 2σ higher than any T/Q host and below ~70 per cent of the SF hosts (see fig. 5 from Nugent et al. 2022). Thus, we cannot conclusively compare the Milky Way with either Q/T or SF hosts alone, but we can conclude that our Galaxy is at least more massive

Table 4. The SGRB sample used in this work. The columns list the host type, the redshift, the projected offset from the host centre in kpc r_h, the projected offset in units of the host's half-light radius r_n, and the fraction of light at the SGRB position f_{light}. Hosts are classified into star-forming (SF), transitioning (T), and quiescent (Q). Host types are taken from Nugent et al. (2022), while the remaining is from Fong et al. (2022).

GRB	Type	z	r_h [kpc]	r_n [r_e]	f_{light}
050509B	Q	0.23	55.19 ± 12.43	2.59 ± 0.58	–
050709	SF	0.16	3.76 ± 0.056	2.00 ± 0.03	0.09 [a]
050724	Q	0.25	2.74 ± 0.08	0.67 ± 0.02	0.33 [a]
051210	SF	2.58	29.08 ± 16.34	5.65 ± 3.17	–
051221A	SF	0.55	2.08 ± 0.19	0.89 ± 0.083	0.65 [a]
060121	–	–	0.97 ± 0.37	0.18 ± 0.069	0.41 [a]
060313	–	–	2.60 ± 0.55	1.39 ± 0.3	0.00 [a]
060614	SF	0.13	0.70 ± 0.79	0.86 ± 0.97	–
061006	SF	0.46	1.39 ± 0.29	0.37 ± 0.077	0.63 [a]
070429B	SF	0.90	6.00 ± 13.44	1.17 ± 2.62	–
070707	–	–	3.25 ± 0.24	1.11 ± 0.083	0.00 [a]
070714B	SF	0.92	12.33 ± 0.87	5.17 ± 0.37	0.00 [a]
070724	SF	0.46	5.52 ± 0.18	1.49 ± 0.048	0.23 [a]
070809	T	0.47	34.11 ± 2.75	9.34 ± 0.75	–
071227	SF	0.38	14.74 ± 0.26	3.08 ± 0.055	0.00 [a]
080503	–	–	7.31 ± 0.24	3.46 ± 0.12	–
090305	–	–	3.49 ± 0.24	1.19 ± 0.083	0.30 [a]
090510	SF	0.90	10.51 ± 2.92	1.66 ± 0.46	0.00 [a]
090515	Q	0.40	76.19 ± 0.16	13.98 ± 0.03	0.00 [a]
091109	–	–	4.22 ± 0.41	1.93 ± 0.19	–
100117A	SF	0.91	1.35 ± 0.32	0.61 ± 0.14	0.54 [a]
130603B	SF	0.36	5.40 ± 0.20	0.71 ± 0.027	0.35 [a]
130912A	–	–	3.90 ± 1.06	1.41 ± 0.38	–
131004A	–	0.72	0.80 ± 0.22	0.25 ± 0.068	–
150101B	Q	0.13	7.36 ± 0.072	0.78 ± 0.0076	0.21 [b]
150424A	–	–	3.41 ± 0.32	1.50 ± 0.14	–
160303A	SF	1.01	15.31 ± 0.90	3.42 ± 0.20	–
160624A	SF	0.48	9.63 ± 6.24	2.37 ± 1.54	–
160821B	SF	0.16	15.74 ± 0.03	4.24 ± 0.008	–
170817A	Q	0.01	2.125 ± 0.001	0.64 ± 0.03	0.54 [c]
200522A	SF	0.55	0.93 ± 0.19	0.24 ± 0.048	0.95 [d]
211106A	–	–	0.79 ± 0.29	0.49 ± 0.18	–
211211A	SF	0.08	7.92 ± 0.029	3.20 ± 0.01	–

Note. **References.** [a]Fong & Berger (2013), [b]Fong et al. (2016), [c]Fong et al. (2017), [d]Fong et al. (2021)

than half of the Q/T hosts, and in the upper quartile of the whole host population. Despite this, it has been suggested that the scale length R_d of the Milky Way disc is anomalously small (Malhotra et al. 1996; Hammer et al. 2007; Licquia, Newman & Bershady 2016; Boardman et al. 2020). Based on the luminosity–velocity–radius (LVR) scaling relation, Licquia, Newman & Bershady (2016) find that the Milky Way R_d is half of the typical value of similar galaxies, which is $R_d \approx 5$ kpc, and that our Galaxy lies farther from the LVR relation than ∼90 per cent of other spiral galaxies, in agreement with Hammer et al. (2007).

These remarks suggest that even if the Milky Way would be representative of the most massive SGRB hosts, the size of its stellar disc could play a role in shifting the r_n distribution of BNS merger to lower values, supporting even more our claim that the agreement we find between BNS mergers and SGRBs is a cosmic coincidence. Nevertheless, we do not investigate the impact of a different R_d since the stochastic spread in the predictions would still be dominant in the KS test.

4.3 Fraction of light

The cumulative distributions of f_{light} for the BNS mergers are shown in the right-hand panels of Fig. 5, together with those for the SGRBs. Similar to the previous cases, the KS test cannot reject the null hypothesis at a significance level below 5 per cent in virtually all realizations. In particular, the null hypothesis is rejected in <0.01 per cent of cases when comparing the BNS mergers to either the whole SGRB sample, to SGRBs with late-types host, or to SGRBs with early-types host. We note that all the f_{light} distribution is skewed to the left, meaning that both BNS mergers and SGRBs do not trace the stellar light, and that they are more likely found in the dimmer pixels. The remarks we made in the previous section about the Milky Way R_d have also implications for the f_{light} distributions of BNS mergers, as a more compact disc would skew the distributions even more to the left. However, we do not test a different R_d as the significant stochastic spread would still dominate in the KS test, as mentioned earlier.

5 SYSTEMATICS

5.1 DM distances

To estimate the distance of J0453+1559, J1411+2551, and J1518+4904, we use their DM together with the model for the free-electron density in the Milky Way from Yao, Manchester & Wang (2017). Different electron-density models however can lead to different distance estimates, therefore we want to test the impact of our specific choice of model. To do this, we compare the results obtained with the model of Yao, Manchester & Wang (2017) to those obtained with the widely used model of Cordes & Lazio (2002).

First of all, we note that all three BNSs with DM distances have merger times greater than the Hubble time, therefore we do not use them for our fiducial models of r_h, r_n, and f_{light}. For this reason, the choice of a specific electron-density model do not impact our results on the BNS merger locations. Regarding the BNS velocities instead, we note that the two different models give similar results. The lognormal distributions fitted to both V and V^{LSR} have the same mean value and 1σ interval regardless of the electron-density model, as reported in Table 3. The angles θ between $\mathbf{V}_t$ and $\mathbf{V}_{t, LSR}$ are also not affected by a different electron-density model, as shown in Fig. 3. We do not show a comparison between the θ distributions from the two electron-models as they overlap and would not be distinguishable. Therefore, we also conclude that our results involving the BNS systemic velocities are not affected by the choice of electron-density model.

5.2 Isotropy assumptions

The toy model discussed in Section 3.2 has not only implications for how representative the BNS sample is of the whole Galactic population, but also for our estimates of the radial velocities V_r. The $\mathbf{V}_t - \mathbf{V}_{t, LSR}$ alignment disfavours the assumption of isotropy under which we obtain V_r for our fiducial model, and also favours kicks with magnitudes less than or equal to the circular velocity, which means that the systemic velocities might still encode the Galactic rotation (although the velocity is not conserved during the orbit).

To check the impact of the isotropy assumption, we perform the analysis in Sections 4.1−4.3 on models employing LSR-isotropic velocities instead of the Galactocentric-isotropic ones, while keeping all the other parameters unchanged. In this variation we compute V_r by de-projecting the residuals $\|\mathbf{V}_t - \mathbf{V}_{t, LSR}\|$ on a random angle, thus
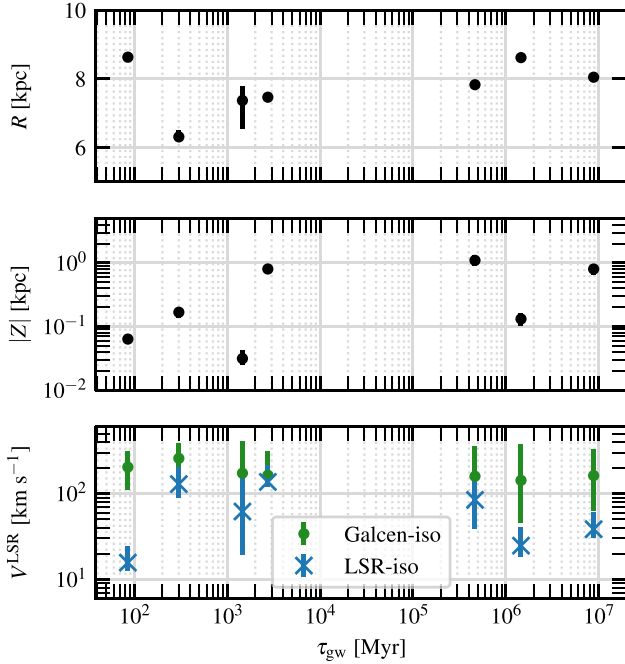
Figure 6. Merger times τ_{gw} against Galactocentric radii R, heights Z, and preculiar velocities V^{LSR} for the BNSs in Fig. 2. The error bars extend from the 16th to the 84th percentiles, and are smaller than the marker when not visible.

simulating the extreme case in which the systemic velocities are the circular velocities at the BNSs locations plus some peculiar velocity. When comparing r_{h}, r_{n}, and f_{light} of BNS mergers to those of SGRBs, the KS test gives the same results as for the fiducial model, namely it cannot reject the null hypothesis below a 5 per cent significance level in virtually all the cases and for all three observables, even though the LSR-isotropic velocities decrease the higher values of r_{h} and increase those of f_{light}. This result reflects the fact that even if Galactocentric- and LSR-isotropic velocities cover different ranges, they are still both close to the circular velocity and well below the escape velocity at the Sun's location, as discussed in Section 3.1. The distributions of observables predicted by the two assumptions are compared in Fig. 7, where we see that the two deviates only for r_{h} and r_{n} at high values.

5.3 Initial conditions

Of the eight confirmed BNSs with measured proper motion, only the five with $\tau_{\mathrm{gw}} < 14$ Gyr have been used to predict the merger locations. We now employ the remaining three to understand how our results depends on the specific initial positions and velocities. To predict the merger locations of these three, though, we cannot not use their true τ_{gw}, since they are at least an order of magnitude greater than the Hubble time (see Table 1) and they might lead to unphysical offsets, i.e. in the case of unbound trajectories. Instead, we use one of the five BNSs τ_{gw} that are below 14 Gyr, motivated by the fact that the τ_{gw} do not show correlation with neither the BNSs positions nor their peculiar velocities, as shown in Fig. 6.

To do this, we repeat the analysis from Sections 4.1−4.3, but this time we swap the initial conditions of each realization with the present-day position and velocity of BNSs randomly drawn among the eight measured proper motions while keeping the τ_{gw} unchanged. The KS test results remain the same of the fiducial model, namely the

test cannot reject the null hypothesis below a 5 per cent significance level in virtually all the cases, for all three observables and for both Galactocentric- and LSR-isotropic velocities. As shown in Fig. 7, this variation affects only the f_{light} distribution skewing it more towards small values.

5.4 Band and resolution of the synthetic image

Lastly, we test our choice of parameters for the fiducial Milky way image. Since the vast majority of SGRBs observables we collect are obtained from *HST* observations, we only test the effects of different redshifts together with different bands, without investigating the impact of PSF and pixel size.

In the fiducial model, we modelled the Milky Way image using $z = 0.5$ and the surface brightness in the I-band μ_I. The choice of redshift is motivated by the median redshift of the SGRB hosts, while the choice of band is motivated by the SGRB hosts being observed mostly in red bands (e.g. *HST F*814*W*). This combination however is unphysical, since the observer-frame I band correspond to the rest-frame V band for a galaxy at $z = 0.5$. To test how it might impact our results, we repeat the analysis from Sections 4.1−4.3 with two different synthetic images, one with $z = 0.2$ and μ_I and the other with $z = 0.7$ and μ_B. These two redshifts mark the 16th and 84th percentiles of the SGRB redshifts. For the higher redshift we use the B band to mimic the bandshift, since light emitted in the B band at $z = 0.7$ would be observed approximately in the I band. For the lower redshift we still use the I band, which is a better approximation than the fiducial model since the observer-frame I band correspond to the rest-frame R band at $z = 0.2$.

When comparing r_{h}, r_{n}, and f_{light} of BNS mergers to those of SGRBs, the KS test gives the same results as for the fiducial model, namely it cannot reject the null hypothesis below a 5 per cent significance level in virtually all the cases and for all three observables. This holds for both images, and for both Galactocentric- and LSR-isotropic velocities. Fig. 7 shows that these variations do not produce significant differences in the predictions.

6 SUMMARY AND CONCLUSIONS

In this work we predicted the merger locations of the Galactic BNSs, and compared them to the locations of SGRBs on their hosts. We compared in particular the projected Galactocentric offsets r_{h}, the host-normalized offsets r_{n}, and the fraction of light f_{light}.

Our fiducial model employs only 5 out of 15 confirmed BNSs, chosen for having measured proper motions and merger times τ_{gw} below the Hubble time. Their present-day Galactocentric positions and velocities are computed through an MC simulation that employs the on-sky positions and proper motions, distances estimated from the BNS DMs, and radial velocities obtained by de-projecting the transverse velocity on to an isotropic orientation. The BNS trajectories are evolved in the Galactic potential starting from the present-day conditions up to τ_{gw}. The merger locations are then analysed on a synthetic image of the Milky Way, as if they were observed from a cosmological distance. The Galaxy model is composed of a bulge/bar plus a double-exponential disc, and the image is made for isotropic viewing angles in the I band, assuming $z = 0.5$, PSF FWHM of 0.1 arcsec, pixel size of 0.05 arcsec px^{-1}, and limiting surface brightness of 25 mag arcsec^{-2}.

When converting the present-day BNS proper motions into Galactocentric transverse velocities $\mathbf{V}_{\mathrm{t}}$, we find that $\mathbf{V}_{\mathrm{t}}$ are similar in magnitude and direction to the transverse velocity of each BNS Local Standard of Rest $\mathbf{V}_{\mathrm{t,LSR}}$ in all but two cases. The similar
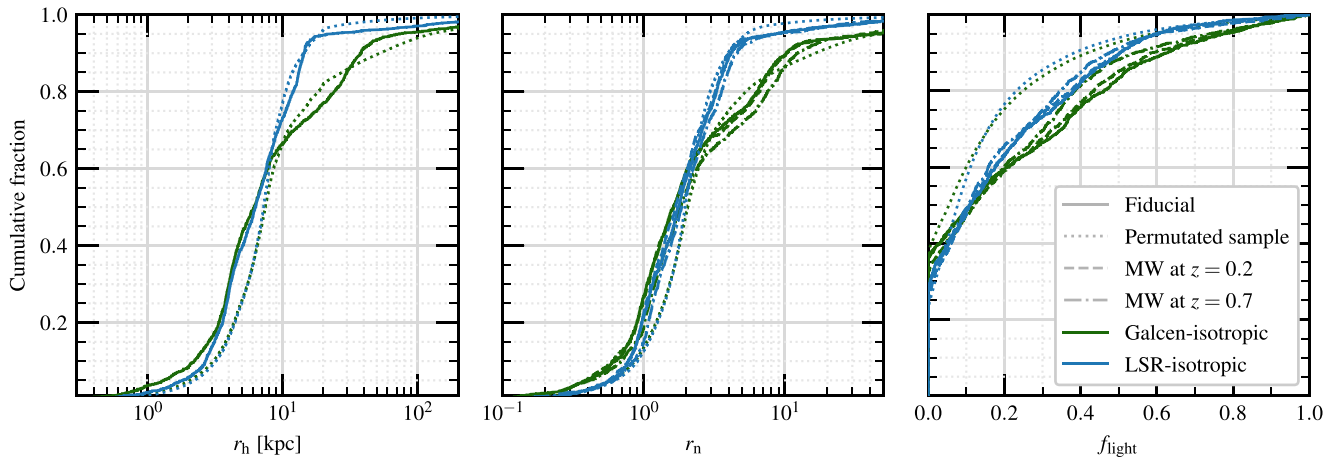
Figure 7. Distributions of observables predicted for the Galactic BNS mergers under several assumptions. Besides the predictions from the fiducial model, the other variations are meant to test different systematic effects that might arise from our methodology. Galactocentric- and LSR-isotropic distributions test the assumption of isotropy used to estimate the BNS radial velocities. Distributions from the permuted sample are obtained by permuting the initial conditions within the BNS that have measured proper motions but no constrain on the merger time, and are meant to test the dependency on the initial conditions within our sample. Distribution for the MW at $z = 0.2$ and $z = 0.7$ are obtained by changing band and angular resolution for the Milky Way image, to test the dependency on the image parameters.

directions suggest that BNSs have systemic velocities **V** which are not isotropically oriented in the Galactocentric frame, but are rather aligned to the LSR velocity. The similar magnitudes suggest instead that BNSs have small peculiar velocities V^{LSR} with respect to the LSR velocity. Using $\mathbf{V}_t$, we compute two different estimates for **V**, one assuming **V** is isotropic, and the other assuming $\mathbf{V}^{\mathrm{LSR}}$ is isotropic. We show that both systemic and peculiar velocities predicted for the observed Galactic BNSs fit a lognormal distribution.

Upon comparison with SGRBs, we find that our predicted BNS merger locations cover the same ranges of r_{h}, r_{n}, and f_{light} as the SGRBs. We compare all the observables predicted for BNS mergers to those of the SGRBs with a KS test, which shows statistically non-significant differences in all cases. This could be attributed to the large spread in our predictions rather than the distributions being intrinsically similar.

We test our results against a range of systematics that might be induced from our methodology. We find that the results from the fiducial model are robust against biases induced by the specific initial conditions of the trajectories, our estimates of the radial velocities, and our choice of parameters for the Milky Way synthetic image. However, we find evidence that our BNS sample is not representative of the whole Galactic population, being biased towards systems that lie at around the same Galactocentric distance of the Sun, and have small peculiar velocities in their LSR. Thus, our sample is likely not representative either of the BNSs born in the inner regions of the Galaxy, or of those dwelling in the outer regions.

Although the connection between BNS mergers and SGRBs is supported by almost two decades of literature, we find that the agreement between the two shown by our analysis is non-trivial. The small peculiar velocities of the BNSs in our sample result in small radial displacements between the start and the end of their trajectories. That is to say, being all located at $R \approx 8$ kpc, they also merge at $R \approx 8$ kpc. Coincidentally, this is also the median offset of SGRBs. Furthermore, although the Milky Way is likely representative of the most massive SGRB hosts, its stellar disc might be more compact than similar spiral galaxies, which could result in lower r_{n} and f_{light}. For this reason, we claim that the agreement we find between Galactic BNS mergers and SGRBs is likely a cosmic

coincidence. Regardless, our results are noteworthy in the fact that we are still able to reproduce the highest values of r_{h} and r_{n}, and the lowest values of f_{light}, for BNSs that start, travel, and merge close to the stellar disc. Also, our results suggest the need of further investigation into how representative the observed Galactic BNSs are compared to the whole Galactic population. A follow-up should analyse the observational biases characterizing the observed BNS sample, and could reveal new implications for the physical processes governing their systemic velocities.

DATA AVAILABILITY

The data underlying this article are available at https://gitlab.com/NicolaGsp/galbns_vs_sgrb.

REFERENCES

Abbott B. P. et al., 2017, ApJ, 848, L12
Agazie G. Y. et al., 2021, ApJ, 922, 35
Andrews J. J., Zezas A., 2019, MNRAS, 486, 3213
Argast D., Samland M., Thielemann F. K., Qian Y. Z., 2004, A&A, 416, 997
Astropy Collaboration, 2013, A&A, 558, A33
Astropy Collaboration, 2018, AJ, 156, 123
Astropy Collaboration, 2022, ApJ, 935, 167
Bagot P., Portegies Zwart S. F., Yungelson L. R., 1998, A&A, 332, L57

[6]http://www.astropy.org

Bartos I., Márka S., 2019, ApJ, 881, L4
Baumgardt H., Hilker M., Sollima A., Bellini A., 2019, MNRAS, 482, 5138
Behroozi P. S., Ramirez-Ruiz E., Fryer C. L., 2014, ApJ, 792, 123
Belczynski K., Perna R., Bulik T., Kalogera V., Ivanova N., Lamb D. Q., 2006, ApJ, 648, 1110
Beniamini P., Piran T., 2016, MNRAS, 456, 4089
Beniamini P., Hotokezaka K., Piran T., 2016, ApJ, 829, L13
Berger E., 2010, ApJ, 722, 1946
Berger E., 2011, New Astron. Rev., 55, 1
Berger E., 2014, ARA&A, 52, 43
Blaauw A., 1961, Bull. Astron. Inst. Neth., 15, 265
Bland-Hawthorn J., Gerhard O., 2016, ARA&A, 54, 529
Bloom J. S., Sigurdsson S., Pols O. R., 1999, MNRAS, 305, 763
Bloom J. S., Kulkarni S. R., Djorgovski S. G., 2002, AJ, 123, 1111
Boardman N. et al., 2020, MNRAS, 491, 3672
Boersma J., 1961, Bull. Astron. Inst. Neth., 15, 291
Bovy J., 2015, ApJS, 216, 29
Bovy J. et al., 2012, ApJ, 759, 131
Bradley L. et al., 2023, photutils v1.8.0
Burgay M. et al., 2003, Nature, 426, 531
Burns E., 2020, Living Rev. Relativ., 23, 4
Cameron A. D. et al., 2018, MNRAS, 475, L57
Champion D. J., Lorimer D. R., McLaughlin M. A., Cordes J. M., Arzoumanian Z., Weisberg J. M., Taylor J. H., 2004, MNRAS, 350, L61
Champion D. J. et al., 2005, MNRAS, 363, 929
Chrimes A. A., Levan A. J., Groot P. J., Lyman J. D., Nelemans G., 2021, MNRAS, 508, 1929
Church R. P., Levan A. J., Davies M. B., Tanvir N., 2011, MNRAS, 413, 2004
Cordes J. M., Lazio T. J. W., 2002, preprint(astro–ph/0207156)
Corongiu A., Kramer M., Stappers B. W., Lyne A. G., Jessner A., Possenti A., D'Amico N., Löhmer O., 2007, A&A, 462, 703
Côté B. et al., 2018, ApJ, 855, 99
Côté B. et al., 2019, ApJ, 875, 106
Cowan J. J., Sneden C., Lawler J. E., Aprahamian A., Wiescher M., Langanke K., Martínez-Pinedo G., Thielemann F.-K., 2021, Rev. Mod. Phys., 93, 015002
Deller A. T., Bailes M., Tingay S. J., 2009, Science, 323, 1327
Deller A. T., Weisberg J. M., Nice D. J., Chatterjee S., 2018, ApJ, 862, 139
Díaz-García S., Salo H., Knapen J. H., Herrera-Endoqui M., 2019, A&A, 631, A94
Eichler D., Livio M., Piran T., Schramm D. N., 1989, Nature, 340, 126
Ferdman R. D. et al., 2014, MNRAS, 443, 2183
Flynn C., Holmberg J., Portinari L., Fuchs B., Jahreiß H., 2006, MNRAS, 372, 1149
Fong W., Berger E., 2013, ApJ, 776, 18
Fong W., Berger E., Fox D. B., 2010, ApJ, 708, 9
Fong W. et al., 2016, ApJ, 833, 151
Fong W. et al., 2017, ApJ, 848, L23
Fong W. et al., 2021, ApJ, 906, 127
Fong W.-f. et al., 2022, ApJ, 940, 56
Fonseca E., Stairs I. H., Thorsett S. E., 2014, ApJ, 787, 82
Fortin F., García F., Chaty S., Chassande-Mottin E., Simaz Bunzel A., 2022, A&A, 665, A31
Freiburghaus C., Rosswog S., Thielemann F. K., 1999, ApJ, 525, L121
Fruchter A. S. et al., 2006, Nature, 441, 463
Fryer C. L., Woosley S. E., Hartmann D. H., 1999, ApJ, 526, 152
Gompertz B. P., Levan A. J., Tanvir N. R., 2020, ApJ, 895, 58
Grady J., Belokurov V., Evans N. W., 2020, MNRAS, 492, 3128
Grindlay J., Portegies Zwart S., McMillan S., 2006, Nat. Phys., 2, 116
Hammer F., Puech M., Chemin L., Flores H., Lehnert M. D., 2007, ApJ, 662, 322
Hobbs G., Lorimer D. R., Lyne A. G., Kramer M., 2005, MNRAS, 360, 974
Hotokezaka K., Beniamini P., Piran T., 2018, Int. J. Mod. Phys. D, 27, 1842005
Jacoby B. A., Cameron P. B., Jenet F. A., Anderson S. B., Murty R. N., Kulkarni S. R., 2006, ApJ, 644, L113
Janssen G. H., Stappers B. W., Kramer M., Nice D. J., Jessner A., Cognard I., Purver M. B., 2008, A&A, 490, 753

Kasen D., Metzger B., Barnes J., Quataert E., Ramirez-Ruiz E., 2017, Nature, 551, 80
Keith M. J., Kramer M., Lyne A. G., Eatough R. P., Stairs I. H., Possenti A., Camilo F., Manchester R. N., 2009, MNRAS, 393, 623
Kirsten F., Vlemmings W., Freire P., Kramer M., Rottmann H., Campbell R. M., 2014, A&A, 565, A43
Kobayashi C. et al., 2023, ApJ, 943, L12
Kramer M. et al., 2006, Science, 314, 97
Lazarus P. et al., 2016, ApJ, 831, 150
Lee W. H., Ramirez-Ruiz E., 2007, New J. Phys., 9, 17
Lee W. H., Ramirez-Ruiz E., van de Ven G., 2010, ApJ, 720, 953
Levan A. J., Wynn G. A., Chapman R., Davies M. B., King A. R., Priddey R. S., Tanvir N. R., 2006, MNRAS, 368, L1
Levan A. J. et al., 2007, MNRAS, 378, 1439
Licquia T. C., Newman J. A., Brinchmann J., 2015, ApJ, 809, 96
Licquia T. C., Newman J. A., Bershady M. A., 2016, ApJ, 833, 220
Lynch R. S., Freire P. C. C., Ransom S. M., Jacoby B. A., 2012, ApJ, 745, 109
Lynch R. S. et al., 2018, ApJ, 859, 93
Malhotra S., Spergel D. N., Rhoads J. E., Li J., 1996, ApJ, 473, 687
Manchester R. N., Hobbs G. B., Teoh A., Hobbs M., 2005, AJ, 129, 1993
Mandhai S., Lamb G. P., Tanvir N. R., Bray J., Nixon C. J., Eyles-Ferris R. A. J., Levan A. J., Gompertz B. P., 2022, MNRAS, 514, 2716
Martinez J. G. et al., 2015, ApJ, 812, 143
Martinez J. G. et al., 2017, ApJ, 851, L29
Matteucci F., Romano D., Arcones A., Korobkin O., Rosswog S., 2014, MNRAS, 438, 2177
McMillan P. J., 2017, MNRAS, 465, 76
Metzger B. D., 2017, Living Rev. Relativ., 20, 3
Metzger B. D., Berger E., 2012, ApJ, 746, 48
Metzger B. D., Quataert E., Thompson T. A., 2008, MNRAS, 385, 1455
Mignani R. P., 2000, A&A, 358, L53
Monari G. et al., 2018, A&A, 616, L9
Mutch S. J., Croton D. J., Poole G. B., 2011, ApJ, 736, 84
Nakar E., 2007, Phys. Rep., 442, 166
Narayan R., Paczynski B., Piran T., 1992, ApJ, 395, L83
Ng C. et al., 2018, MNRAS, 476, 4315
Nugent A. E. et al., 2022, ApJ, 940, 57
O'Connor B. et al., 2022, MNRAS, 515, 4890
Oke J. B., Gunn J. E., 1982, PASP, 94, 586
Perets H. B., Beniamini P., 2021, MNRAS, 503, 5997
Perna R., Belczynski K., 2002, ApJ, 570, 252
Peters P. C., 1964, Phys. Rev., 136, 1224
Pian E. et al., 2017, Nature, 551, 67
Piffl T. et al., 2014, A&A, 562, A91
Portegies Zwart S. F., Yungelson L. R., 1998, A&A, 332, 173
Qin B., Wu X.-P., Chu M.-C., Fang L.-Z., Hu J.-Y., 1998, ApJ, 494, L57
Rastinejad J. C. et al., 2022, Nature, 612, 223
Reid M. J. et al., 2019, ApJ, 885, 131
Ridolfi A., Freire P. C. C., Gupta Y., Ransom S. M., 2019, MNRAS, 490, 3860
Robin A. C., Reylé C., Derrière S., Picaud S., 2003, A&A, 409, 523
Rosswog S., Liebendörfer M., Thielemann F. K., Davies M. B., Benz W., Piran T., 1999, A&A, 341, 499
Salafia O. S., Colombo A., Gabrielli F., Mandel I., 2022, A&A, 666, A174
Sarin N., Lasky P. D., Vivanco F. H., Stevenson S. P., Chattopadhyay D., Smith R., Thrane E., 2022, Phys. Rev. D, 105, 083004
Shen S., Cooke R. J., Ramirez-Ruiz E., Madau P., Mayer L., Guedes J., 2015, ApJ, 807, 115
Stairs I. H., Thorsett S. E., Taylor J. H., Wolszczan A., 2002, ApJ, 581, 501
Stovall K. et al., 2018, ApJ, 854, L22
Swiggum J. K. et al., 2015, ApJ, 805, 156
Symbalisty E., Schramm D. N., 1982, Astrophys. Lett., 22, 143
Tauris T. M. et al., 2017, ApJ, 846, 170
Thompson C., Duncan R. C., 1995, MNRAS, 275, 255
Troja E., King A. R., O'Brien P. T., Lyons N., Cusumano G., 2008, MNRAS, 385, L10
Tunnicliffe R. L. et al., 2014, MNRAS, 437, 1495

Urquhart J. S., Figura C. C., Moore T. J. T., Hoare M. G., Lumsden S. L., Mottram J. C., Thompson M. A., Oudmaijer R. D., 2014, MNRAS, 437, 1791

van de Voort F., Quataert E., Hopkins P. F., Kereš D., Faucher-Giguère C.-A., 2015, MNRAS, 447, 140

van der Walt S. et al., 2014, PeerJ, 2, e453

van Leeuwen J. et al., 2015, ApJ, 798, 118

Verbiest J. P. W., Weisberg J. M., Chael A. A., Lee K. J., Lorimer D. R., 2012, ApJ, 755, 39

Verbunt F., Igoshev A., Cator E., 2017, A&A, 608, A57

Vigna-Gómez A. et al., 2018, MNRAS, 481, 4009

Virtanen P. et al., 2020, Nat. Methods, 17, 261

Voss R., Tauris T. M., 2003, MNRAS, 342, 1169

Wang X. et al., 2021, ApJ, 923, 219

Wegg C., Gerhard O., 2013, MNRAS, 435, 1874

Wehmeyer B., Pignatari M., Thielemann F. K., 2015, MNRAS, 452, 1970

Weisberg J. M., Huang Y., 2016, ApJ, 829, 55

Weisberg J. M., Nice D. J., Taylor J. H., 2010, ApJ, 722, 1030

Willmer C. N. A., 2018, ApJS, 236, 47

Yao J. M., Manchester R. N., Wang N., 2017, ApJ, 835, 29

Yu S.-Y., Ho L. C., 2020, ApJ, 900, 150

Yu S.-Y., Ho L. C., Barth A. J., Li Z.-Y., 2018, ApJ, 862, 13

Zemp M., Ramirez-Ruiz E., Diemand J., 2009, ApJ, 705, L186

Zevin M., Kelley L. Z., Nugent A., Fong W.-f., Berry C. P. L., Kalogera V., 2020, ApJ, 904, 190

This paper has been typeset from a TEX/LATEX file prepared by the author.